

# GA-BASED LASER SPECKLE PATTERN DIGITAL IMAGE CORRELATION METHOD FOR SURFACE STRAIN MEASUREMENTS

ARKA DAS<sup>1</sup>, EDUARDO DIVO<sup>1</sup>, FAISAL MOSLEHY<sup>2</sup> & ALAIN KASSAB<sup>2</sup>

<sup>1</sup>Mechanical Engineering Department, Embry-Riddle Aeronautical University, USA.

<sup>2</sup>Mechanical and Aerospace Engineering Department, University of Central Florida, USA.

## ABSTRACT

This article introduces an innovative technique that integrates a genetic algorithm (GA)-based digital image correlation with laser speckle photography for the estimation of surface displacements in structures. The images (before and after deformation) are digitized using a digital camera, and the grayscale intensity matrices are read and processed by an image processing algorithm. The two matrices of the images are then inputted into GA-based optimizer that utilizes an advanced cross-correlation fitness function to approximate the surface displacements. Furthermore, the surface strains are computed from the displacements using radial basis function differentiation and interpolation. The computed displacements are compared with simulated results obtained by the boundary element method. Close agreement between the two results proves the validity of the developed noncontact technique for accurately estimating surface displacements and strains. These experimentally estimated displacements can further be used in an inverse technique to detect and characterize subsurface cavities in structures.

*Keywords:* boundary element method, genetic algorithm, laser speckle pattern, RBF interpolation, surface strain.

## 1 INTRODUCTION

The surface strain is an important material property that needs to be measured to understand the mechanical behavior of the material under a specific loading condition, as mentioned by Manthey and Lee [1]. With the advancement in the field of the automated stereo vision system, it has been possible to measure the surface strain value of an object using various imaging techniques. Vogel and Lee [2] explained that the accuracy of such automated vision-based measurement techniques much depend on multiple factors: number of pictures, camera resolution, the internal geometry of camera, accuracy of grid pattern, etc. Studies by Theocaris and others [3–9] were resourceful in the description of various coherent optical light methods and noncoherent optical light methods. The Moiré technique makes it feasible to study the strain values with the normal eye. Takaki *et al.* [10] explained the process of obtaining higher accuracy in strain measurements by using a digital camera. In recent years, Moiré interferometers with high magnification have been developed [11, 12]. One of the crucial limiting factors of this technique is the accurate detection of the depth of field. Holographic interferometry stores multiple wave fronts to perform interferometry. Trolinger [13] invented a multi-exposure technique for real-time holographic interferometry, which mitigated the problem of fringe formation depending on either rapid or too slow movement of the object.

The principle behind speckle interferometry is interference between two coherent light rays, as described by Rastogi [14]. Speckle interferometry is classified into specklegram, speckle decorrelation, and speckle pattern shearing interferometry (shearography). Specklegram technique is used to measure strain and in-plane movement of surfaces. Speckle decorrelation method is used to visualize surface movement when there is a speckle separation during a double exposure. Shearographic interferometry is resilient to the environment and it finds its application in measuring surface displacement, as discussed by Francis *et al.* [15].

A more straightforward technique using the digital image correlation (DIC) method was developed in the early 1980s for measuring the in-plane deformations of an object [16, 17]. Sutton *et al.* [18] explained the versatility of DIC and its applications in different domains of engineering. The main principle behind DIC is to compare images of an object at different stages during deformation. Different DIC solutions are available to obtain sub-pixel resolution based on Newton–Raphson iteration, a nonlinear optimization technique, genetic algorithms (GAs), etc. as explained by Bing *et al.* [19]. Results obtained through DIC is dependent on the spatial and temporal resolution of the imaging system and homogeneity of the material, as discussed by Mudassar and Butt [20]. Studies by Zhang and others [21–26] were resourceful in elaborating on the existence of a nonlinear relationship between the actual displacement of the object plane and the displacement of speckle pattern at the image plane and establishing the geometric distortion correction factor that must be applied to obtain accurate in-plane displacements.

To this end, we developed an image domain decomposition approach to laser speckle photography (LSP) for deformation measurements. In this article, a GA was utilized to determine the motion of the center of pixel groupings by maximizing a simplified cross-correlation expression. The whole specimen deformation was subsequently reconstructed using radial basis function interpolation, and the strains were found by radial basis function (RBF) differentiation. The experimentally obtained displacement results utilizing RBF-GA-based domain decomposition technique were validated against simulations conducted by using an in-house code developed on boundary element method (BEM).

## 2 METHOD

### 2.1 Laser speckle pattern setup

Gauvin and others [27–30] described three different categories of speckle patterns, i.e. natural texture, artificial speckle, and laser speckle patterns. The application of the LSP involves the impingement of a coherent laser beam onto a rough surface that produces the laser speckle pattern, and these laser speckle particles are relative to the wavelength of the laser and surface roughness of the specimen. The ideal surface texture of the object to be studied should be isotropic. Laser speckles are formed when laser irradiates the surface of the object leading the surface to scatter numerous coherent wavelets. These wavelets interfere with each other in space around the object. When the phase difference between the scattered wavelets satisfies constructive interference, wavelets form a bright spot. When wavelets satisfy destructive interference, dark spots are formed. Bright and dark spots formed by these wavelets are distributed in a random fashion around the surface. The bright and dark spots imaged in an image acquisition device gives rise to laser speckle [31, 32]. The procedure involves the application of a random speckle pattern to a surface of interest, and then capturing consecutive digital images of the surface before and after deformation has occurred. Finally, the two captured images are compared to compute the displacement for the surface. Figure 1 shows the schematic of the experimental setup. In general, LSP requires less mechanical stability compared with holographic interferometry. To accurately measure in-plane translation, strain rotation, vibration, and out-of-plan rotation, the LSP has been used [33].

When a coherent beam generated from a laser source impinges at a point on the specklegram, a diffraction cone with an angle  $\alpha$  will be formed at the observation screen by the two speckle patterns regulated by parallel fringes. The screen is at a distance ‘Z’ behind the

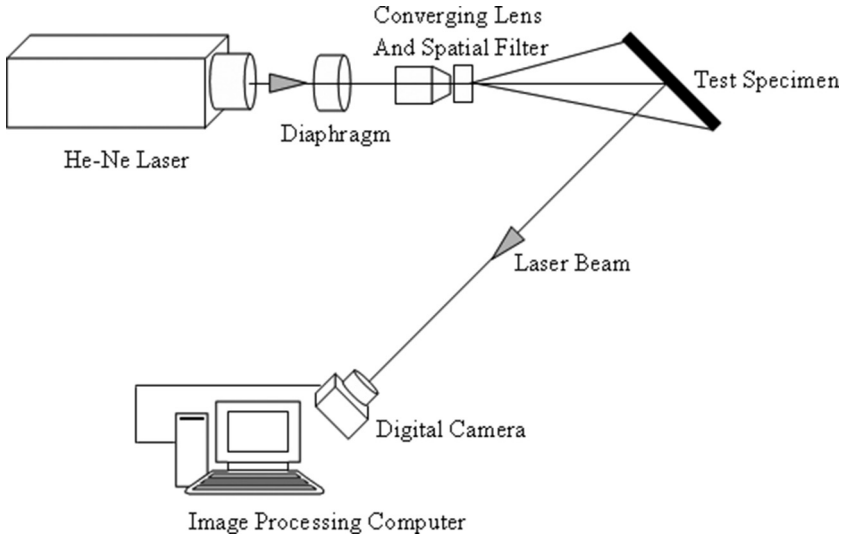


Figure 1: Schematic of the experimental setup.

specklegram as shown in Fig. 2. Fringe patterns created are equidistant and similar to Young’s fringes. A point-by-point record for displacement is obtained when the spacing of the fringes and orientation can be measured.  $u$  and  $v$  components of displacement are calculated by

$$u = U \cos \theta \tag{1}$$

$$v = U \sin \theta \tag{2}$$

$$U = \frac{\lambda Z}{Md} \tag{3}$$

where  $\theta$  is the angle between the horizontal and normal to the fringe,  $\lambda$  is the wavelength of the laser beam,  $Z$  is the distance between specklegram and observation plane,  $M$  is the magnification, and  $d$  is the spacing between fringe. Magnification is the ratio of image to object size.

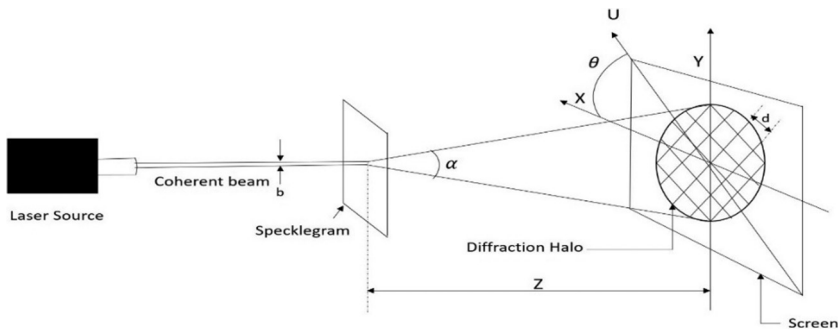


Figure 2: Point-wise filtering for in-plane displacement measurements.

## 2.2 Domain decomposition technique

Usually, various kinds of image matching techniques are used with the LSP to compute deformation of a surface. Depending on the type of in-plane movement of the gray value subset, suitable type of image matching technique is chosen, e.g. differential method, template matching, and subset or polynomial shape function. Fraley and others [34–37] gave an in-depth insight into different types of correlation methods and optimizing algorithms based on evolutionary methods for DIC.

In this article, an effective domain decomposition method was developed based on the cross-correlation of the gray value of the subset. Assume a speckle pattern is created on a given surface and an image is captured as shown in Fig. 3a. Depending on the loading condition, a point of interest on this image undergoes motion. When a region around this point is selected, the region may undergo displacement and strain so that the location and shape of the region are shown as a parallelogram as shown in Fig. 3b. Now the point of interest is the center of the parallelogram.

The method for comparing the two subsets (to determine the displacement vector  $\vec{u}$ , see Fig. 4) is commonly given by the cross-correlation coefficient,  $C$ :

$$C(u, v) = \frac{\int_{\Delta M^*} f(x, y) f^*(x+u, y+v) dA}{\sqrt{\left( \int_{\Delta M} f^2(x, y) dA \right) \left( \int_{\Delta M^*} f^{*2}(x+u, y+v) dA \right)}} \quad (4)$$

where  $\Delta M$  is the subset in the undeformed image,  $\Delta M^*$  is the subset in the deformed image, and  $f(x, y)$  is the gray level of speckle at a point (pixel).

The values of  $u$  and  $v$  which maximize  $C$  are the local deformation (displacement components) for the selected subset. The objective of the image correlation process is to obtain the values for the subset under investigation and repeat for all subsets in a given region to obtain the whole field deformation profile. The above is then implemented as

$$C(u, v) = \frac{\sum_{\Delta M^*} (\text{graylevels})(\text{graylevels})^*}{\sqrt{\sum_{\Delta M} (\text{graylevels})^2 \sum_{\Delta M^*} (\text{graylevels})^{*2}}} \quad (5)$$

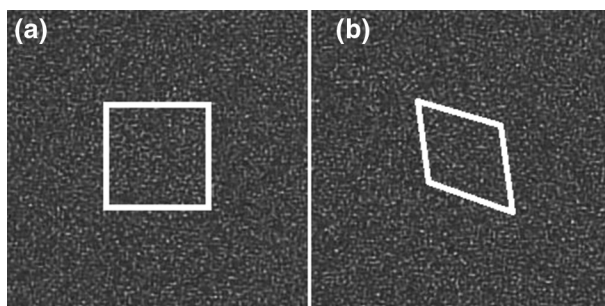


Figure 3: (a) Undeformed image and (b) actual deformed image.

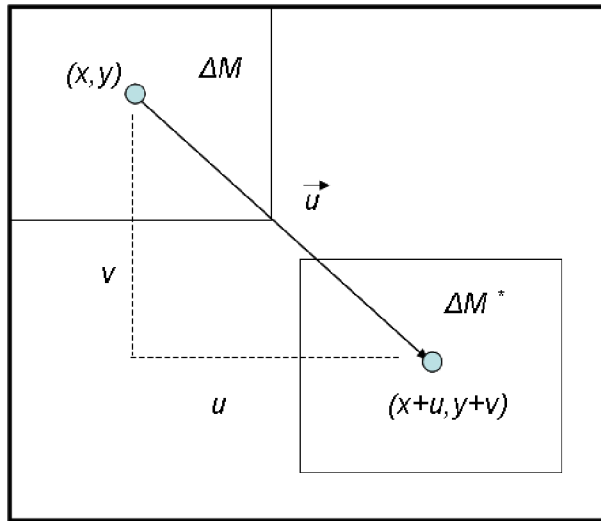


Figure 4: Model utilized in this study: motion of the center of a grouping of pixels.

To account for actual deformations and not translation alone, the above correlation should at least be augmented by first derivatives. Since a domain decomposition approach is adopted, the regions under deformation are significantly reduced in size with each subdomain viewed with the full resolution of the camera as illustrated in Fig. 5. For each group of pixels, the values of  $u$  and  $v$  that maximize the correlation in eqn (4) are determined by a GA. The image of the whole specimen is then reconstructed via RBF interpolation of the motion of each pixel grouping.

### 2.3 Genetic algorithm

The GA optimization begins by setting up a set of random set of possible solutions, called the population, with a fixed set of individuals. Each individual in the population is defined by its optimization variables that are represented by a bit string or chromosome. In this case, an

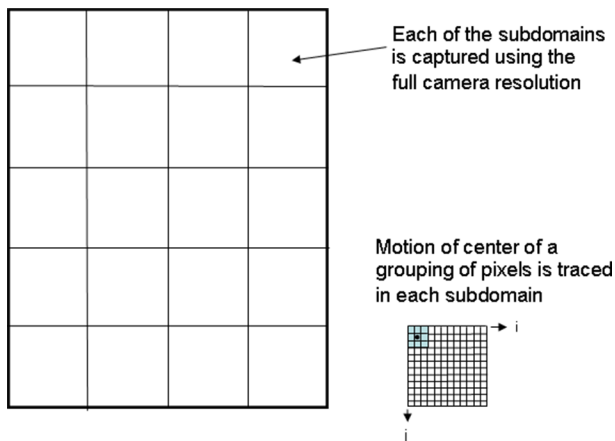


Figure 5: Domain decomposition of the image.

objective function  $Z(u,v) = C(u,v)$  is evaluated for individuals in the current population to define their fitness or their probability of survival. A selection operator is applied to the population to determine and select individuals who are going to pass information during the mating process with rest of the individuals in the population. This mating process is called the crossover operator. By doing this process, the genetic information present within the best individuals combines to form the offspring. Also, a mutation operator randomly affects the information obtained during the mating process. This mutation is a critical step for continuous improvement. During every single iteration of GA, the process of selection, crossover, and mutation is used to update the population.

In nature, an organism has some properties that are described by a string of genes present in the chromosomes. Therefore, haploid model using binary vector is adopted in this article to model a given chromosome. The number of design variables and the required precision of each design variable dictate the length of the vector. Each design variable is bound to maximum and minimum values, and in this process the precision of the variable is determined. During discretization, the number of divisions used is an integer power of two. This allows easy mapping from binary strings to real numbers and vice versa. Each individual is equipped with a value objective function that corresponds to the given set of design variables. This value is the measure of the fitness of the individual design. Poorly fit designs are not discarded in GA, and they are kept to provide genetic diversity in the evolution of a population. Genetic diversity is required for the forward movement of the population during mating, crossover, and mutation processes that characterize the GA [38].

In this developed GA algorithm, the population size is fixed which initiates the algorithm in all chromosomes. Operation is performed by assigning 0 or 1 in random orders for each bit in each of the chromosome. After the population is initialized with random values, the fitness of each individual is evaluated by computing the value of the objective function. The probability of being a selected individual for mating is calculated as the ratio between the value of the fitness function of every individual and the sum of all fitness function values. This is given by

$$P_{selected} = \frac{Fitness(v_i)}{\sum_{i=1}^{population-size} Fitness(v_i)} \quad (6)$$

$v_i$  is the  $i$ th member of the population, and  $Fitness(v_i)$  is a measure of the fitness of that member under its currently evolved parameter set configuration. A weighted Roulette wheel is generated, and every member of the current population is assigned a portion of the wheel that is in proportion to its probability of being selected. The wheel is spun as many times as there are individuals in the population to select which members mate. Some individuals can be selected more than once, and hence the best chromosomes get more copies, the average stays even, and the worst dies off. After selection is applied, crossover and mutation occur to the resulting offspring which further enlarge genetic diversity in the population. Other probabilities that are referred to the description of GA adopted in this article are computed in an analogous fashion as the selection probability.

The probability of crossover  $P_c$  is a parameter that determines the expected population of chromosomes ( $P_c \times population\ size$ ) that undergo crossover operation. This operation can be executed in two steps: (1) pairs of individuals obtained by a random selection based on the probability of crossover and (2) generation of a random number between the first and last positions of binary vector to indicate the location of the crossing point that delineates the

location about genetic information that is interchanged between two chromosomes. The mutation operator is the final operator implemented. The probability of mutation  $P_m$  provides the expected number of mutated bits. All chromosomes in the entire population have an equal opportunity to undergo mutation. The process is implemented by a generation of random numbers between 0 and 1 for each bit in the chromosome. A bit is mutated if the generated number is smaller than the bit.

Following selection, crossover, and mutation, the new population is ready for its next evolution until the convergence criteria 'fitness' is reached. It is the very nature of the binary representation of the design variables of the objective function and the random search process which provides yet another but implicit degree of regularization in this optimization process. The sensitivity of the objective function can be tuned depending on the size of each element of the chromosome. Thus, low bit representation is insensitive to large variations in input (regularized but may lead to poor solution due to low resolution), while high bit representation is sensitive to large variations in input (not regularized and therefore may lead to poor solution as well). There is a range of bit size which produces a regularized and sensitive response leading to stable solutions.

The GA used to obtain results presented in this article, and the following parameters are considered: population size of 50 individuals/generation, a string of 10 bits to define each parameter with each individual, two offsprings for every mating, 1% probability of mutation, and 70% probability of crossover. Population growth is not allowed, and this parameter combination has proven to yield accurate and efficient optimization results for different studies carried out by Divo and others [39–41, 49].

#### 2.4 RBF interpolation and strain computation

The RBF interpolation is defined by a set of data centers,  $x_c$ , comprised of points distributed throughout the entire domain and its boundary which need not be uniformly distributed. These data centers work as collocation points for the localized expansion of variables of interest in the domain and on its boundary.

A localized expansion over a group or topology of influence points,  $NF$ , around each data center is sought such that:

$$\phi(x) = \sum_{j=1}^{NF} a_j \chi_j(x) + \sum_{j=1}^{NP} a_{j+NF} P_j(x) \quad (7)$$

Variable  $\phi$  will take the values of  $u$  or  $v$  based on the application,  $x$  indicates the  $x$ - $y$  pair of coordinates at a given point,  $a_j$  indicates the unknown expansion coefficients,  $\chi_j$  are the RBF expansion functions,  $NP$  is defined as the number of additional polynomial functions,  $P_j(x)$ , added to the expansion such that constant and linear fields are retrieved exactly. RBF utilized belongs to the family of Hardy multiquadrics [42]:

$$\chi_j(x) = \left[ r_j^2(x) + c^2 \right]^{n - \frac{3}{2}} \quad (8)$$

Here  $n$  is defined as a positive exponent,  $c$  is defined as the shape parameter, and  $r_j(x)$  is the Euclidean distance from  $x$  to  $x_j$ . In this article,  $n = 1$  is utilized, which yields the inverse multiquadrics whose behavior is extensively studied in the literature [43, 44]. The behavior of the interpolation and accuracy of its derivative is controlled by the shape parameter,  $c$ . The

computed derivative field becomes smoother when the shape parameter is large for a specific expansion over a given set of data centers. The magnitude of the shape parameter cannot be increased without bound as the expansion functions become flatter and the collocation coefficient matrix becomes ill-conditioned. To determine each value of the shape parameter used in every expansion at different local topologies, a simple optimization search is employed. The ratio of the average distance between data centers in a given topology to the number of points in that topology is taken as the initial guess for  $c$ .

The localized expansion approach [45, 46] decreases the computational burden on global RBF interpolation by expanding the field variable locally around each data center to interpolate and to obtain its derivatives. By this approach, a small interpolation matrix is generated for each data center rather than having a large interpolation matrix obtained by global methods.

By performing a circular search around each data center, the region of influence or the localized topology is selected. The search is automated in a way that a minimum number of points will be included and additional criteria are met, such as including all directions around the internal data centers, as shown in Fig. 6.

The following matrix–vector form is obtained after the collocation of the field variable at the points within the localized topology:

$$\{\phi\} = [C]\{a\} \Rightarrow \{a\} = [C]^{-1}\{\phi\} \tag{9}$$

where the matrix  $[C]$  and the vector  $\{\phi\}$  are composed as:

$$[C] = \begin{bmatrix} \chi_1(x_1) & \dots & \chi_{NF}(x_1) & P_1(x_1) & \dots & P_{NP}(x_1) \\ \cdot & \cdot & \cdot & \cdot & \cdot & \cdot \\ \chi_1(x_{NF}) & \dots & \chi_{NF}(x_{NF}) & P_1(x_{NF}) & \dots & P_{NP}(x_{NF}) \\ P_1(x_1) & \dots & P_1(x_{NF}) & 0 & \dots & 0 \\ \cdot & \cdot & \cdot & \cdot & \cdot & \cdot \\ P_{NP}(x_1) & \dots & P_{NP}(x_{NF}) & 0 & \dots & 0 \end{bmatrix} \text{ and } \{\phi\} = \begin{Bmatrix} \phi(x_1) \\ \cdot \\ \phi(x_{NF}) \\ 0 \\ \cdot \\ 0 \end{Bmatrix} \tag{10}$$

Evaluating eqn (7) for the field variable at the data center  $x_c$  and substituting eqn (9) lead to the following form:

$$\phi(x_c) = \{\chi(x_c)\}^T [C]^{-1}\{\phi\} = \{\psi(x_c)\}^T \{\phi\} \tag{11}$$

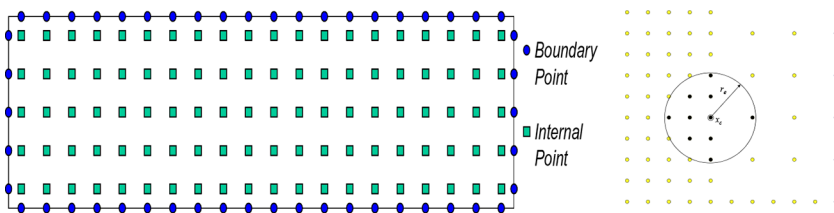


Figure 6: Point collocation of data centers with uniform spacing, and collocation topology for nonuniform spacing.

Field variable derivatives at the data centers can be computed directly by differentiating the RBF expansion of the field variable in eqn (7). For example, consider any linear differential operator  $L$ :

$$L\phi(x_c) = \sum_{j=1}^{NF} a_j L\chi_j(x_c) + \sum_{j=1}^{NP} a_{j+NF} LP_j(x_c) \tag{12}$$

where  $x_c$  is the data center of the topology. Thus, in matrix–vector form:

$$L\phi_c = \{L_c\}^T \{a\} \Rightarrow L\phi_c = \{L_c\}^T [C]^{-1} \{\phi\} \Rightarrow L\phi_c = \{L\}^T \{\phi\} \tag{13}$$

where the vector  $\{L_c\}$  is composed by:

$$\{L_c\} = \begin{pmatrix} L\chi_1(x_c) \\ \vdots \\ L\chi_{NF}(x_c) \\ LP_1(x_c) \\ \vdots \\ LP_{NP}(x_c) \end{pmatrix} \tag{14}$$

An alternative approach for calculating the field variable derivatives is through the use of RBF-enhanced finite differencing (RBF-FD). This approach reduces instabilities associated with directly differentiating the RBF expansion (see [45]). In this case, RBF interpolation is utilized to approximate the field variable at locations on a finite difference stencil at the data centers. For example, a second-order central difference evaluation of the first  $x$ -derivative at the data center  $x_p$  involves interpolating the field variable at locations  $a$  and  $b$  as shown in Fig. 7. Equation (7) is then applied on a topology surrounding these two points, leading to:

$$\phi(x_a) = \{\psi(x_a)\}^T \{\phi\}_a \tag{15}$$

$$\phi(x_b) = \{\psi(x_b)\}^T \{\phi\}_b \tag{16}$$

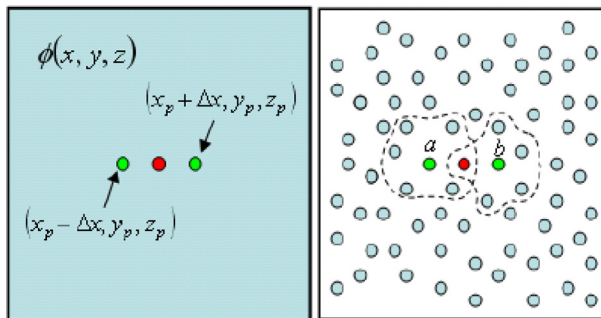


Figure 7: Differentiation stencil and local topology for radial basis function-enhanced finite differencing.

where  $\{\psi(x_a)\}$  is the interpolating weight vector and  $\{\phi\}_a$  is the nodal value vector associated with point  $a$ , and  $\{\psi(x_b)\}$  is the interpolating weight vector and  $\{\phi\}_b$  is the nodal value vector associated with point  $b$ .

Therefore, substituting these virtual point expressions into a second-order accurate central difference of the first  $x$ -derivative at the data center  $x_c$  leads to:

$$\frac{\partial\phi}{\partial x} = \left\{ \frac{1}{2\Delta x} \{\psi(x_a)\}^T \quad \frac{-1}{2\Delta x} \{\psi(x_b)\}^T \right\}^T \begin{Bmatrix} \{\phi_a\} \\ \{\phi_b\} \end{Bmatrix} = \{L_{c,x}\}^T \{\phi\} \tag{17}$$

For any other derivative of interest, this is readily extended. Using the RBF-ND or RBF-FD approaches, the field variable derivatives are evaluated at every one of the data centers  $x_c$ . This can be accomplished by an inner product of two small vectors:  $\{L_c\}$  that can be pre-built and stored and  $\{\phi\}$  that contains the field variable values at the surrounding RBF points within the topology of the data center  $x_c$ . In this article, all derivatives in the calculation of strain fields are computed using the RBF-FD:

$$\varepsilon_x = \frac{\partial u}{\partial x}, \varepsilon_y = \frac{\partial v}{\partial y}, \gamma_{xy} = \frac{\partial u}{\partial y} + \frac{\partial v}{\partial x} \tag{18}$$

### 2.5 Boundary element method formulation

In the single-domain direct boundary element method, with a given domain  $\Omega$ , parameters such as displacement, traction, and stresses can be computed on the boundary  $\Gamma$ . Displacement and stress can be computed inside the domain by obtaining the numerical solution of a boundary integral equation as mentioned in Brebbia *et al.* [47].

The equilibrium equation governs the state of stress in the solid body as follows:

$$\frac{\partial\sigma_{ij}}{\partial x_j} = -b_i \tag{19}$$

The strain tensor is given by:

$$e_{ij} = \frac{1}{2} \left( \frac{\partial u_i}{\partial x_j} + \frac{\partial u_j}{\partial x_i} \right) \tag{20}$$

In a Hookean solid, the stress tensor is linearly related to the strain tensor as:

$$\sigma_{ij} = \frac{2\mu\nu}{1-\nu} \delta_{ij} e_{ii} + \mu e_{ij} \tag{21}$$

where  $\sigma_{ij}$  is the stress tensor,  $u_i$  is the displacement vector,  $\delta_{ij}$  is the Kronecker delta,  $\mu$  is the shear modulus, and  $\nu$  is the Poisson's ratio. The boundary traction  $t_i = \sigma_{ij} n_j$  is used to define the normal boundary condition with  $n_j$  denoting the boundary outward-drawn unit normal vector. Combining eqns (19) and (21) leads to the following Navier's equation that expresses equilibrium in terms of displacement:

$$\mu \frac{\partial^2 u_i}{\partial x_j \partial x_j} + \frac{\mu}{(1-2\nu)} \frac{\partial^2 u_j}{\partial x_i \partial x_j} = -b_i \tag{22}$$

In a well-posed boundary value problem, either the displacement  $u_i = \bar{u}_i$  on boundary  $\Gamma_u$  or the traction  $t_i = \bar{t}_i$  on boundary  $\Gamma_t$  must be prescribed on each part of the boundary.  $\Gamma_u \cup \Gamma_t = \Gamma$  is the boundary of the domain  $\Omega$ . In the formulation of BEM based on Somigliana identity, an integral relation between the displacements  $u_i^p$  in a collocation point 'p' and the displacements  $u_i$  and tractions  $t_i$  on all boundary  $\Gamma$  is derived. Body force term  $b_i$  is related through a domain integral as follows:

$$c_{ij}^p u_i^p + \oint_{\Gamma} H_{ij} u_i d\Gamma = \oint_{\Gamma} G_{ij} t_i d\Gamma + \oint_{\Omega} G_{ij} b_i d\Omega \tag{23}$$

The fundamental solution of the above equation in terms of displacement and traction is obtained from  $G_{ij}$  and  $H_{ij}$ , while  $c_{ij}^p$  is a geometric constant which takes the values 0, 1/2, and 1 based on the following conditions:

$$c_{ij}^p = 0 \text{ if } p \in \Omega \tag{24}$$

$$c_{ij}^p = 1/2 \text{ if } p \notin \Omega \tag{25}$$

$$c_{ij}^p = 1 \text{ if } p \in \Gamma \tag{26}$$

The fundamental solutions for the two-dimensional (2D) case are

$$G_{ij} = \frac{1}{8\pi\mu(1-\nu)} \left[ (4\nu-3)\delta_{ij} \ln r + \frac{\partial r}{\partial x_i} \cdot \frac{\partial r}{\partial x_j} \right] \tag{27}$$

$$H_{ij} = \frac{-1}{4\pi(1-\nu)r} \left[ 2 \left( \frac{\partial r}{\partial n} \frac{\partial r}{\partial x_i} \frac{\partial r}{\partial x_j} \right) + (1-2\nu) \times \left( \delta_{ij} \frac{\partial r}{\partial n} + \frac{\partial r}{\partial x_i} n_j - \frac{\partial r}{\partial x_j} n_i \right) \right]$$

The above equation can be discretized in the standard BEM form as

$$[H]\{U\} = [G]\{t\} + \{b\} \tag{28}$$

By introducing boundary conditions into the vectors  $\{U\}$  and  $\{t\}$ , the above equation leads to a system of simultaneous linear equations which is of the form  $[A]\{x\}=\{B\}$ , and this is obtained by rearranging eqn (28) by taking known quantities to the right-hand side and unknown to the left-hand side as described in the studies by Kassab and others [33], [48, 49].

### 3 EXPERIMENTAL PROCEDURE AND DATA COLLECTION

For the experimental setup, a Plexiglas block specimen of 168 mm in width, 250 mm in length, and 4.8 mm in thickness, with two circular holes with diameters of 35 and 40 mm was fabricated and tested. A clear divergent laser beam was installed to illuminate the Plexiglas specimen. This was obtained by adjusting the translation stage that held the spatial filter. Other optical instruments were clamped onto a table as shown in Fig. 8. The Plexiglas specimen was clamped on a loading frame and 500 lb (2224.11 N) of the tensile load was applied. Two images covered with laser speckles were captured using a digital camera. The first image was under the deformed state with a load of 500 lb and the second image was captured when the tensile load was reduced to 100 lb (444.82 N).

The digital camera used in this experiment can give a full resolution of 2832 × 2128 pixels at its full zoom. Upon cropping the images to size, the resolution obtained was 0.125 mm/pixel. Figure 9 indicates the gray-level distribution, where the intensity distribution of light reflected by the specimen is stored as gray levels (set of nondimensional numbers) in a

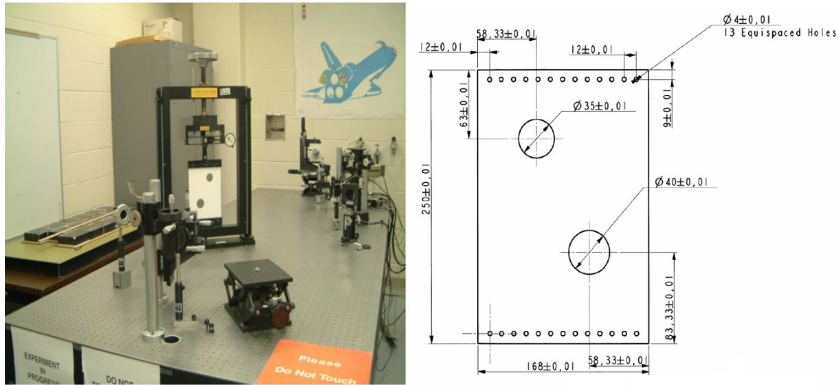


Figure 8: Photograph of the experiment setup and details of the test specimen.

computer via an appropriate information transfer. The gray-level distribution indicates the brightness of pixels in the domain. The minimum gray level is 0 and the maximum gray level depends on the depth of the digitized image. For example, for an 8-bit depth image it is 255. Hence in a gray scale of such image, a pixel can take on any value between 0 and 255. Preliminary BEM results showed that the maximum deformation of the Plexiglas specimen would be in the order of 0.3 mm, and this corresponds to less than 3 pixels. The low-resolution image provided poor output for surface displacements when initial runs of image correlation were done using the GA.

The low-resolution problem was overcome by decomposing the Plexiglas specimen into equally spaced subdomains and then capturing an image for each subdomain separately at full zoom and highest resolution. Figure 10a and 10b shows the surface of the Plexiglas specimen divided into 20 subdomains, each identified by its own row and column (starting at 11: top left-hand side subdomain).

The camera was mounted and firmly clamped on the isolation mount and was kept 250 mm away from the Plexiglas specimen. The camera at its highest resolution was zoomed to focus on the first subdomain (11). This process was repeated for each of the regions (11–54) under

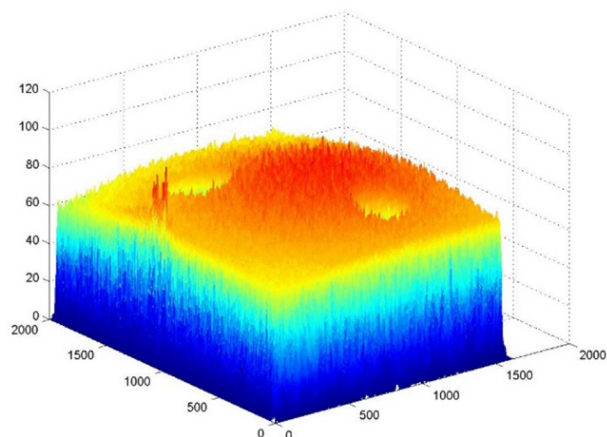


Figure 9: Gray-level distribution of specimen covered by laser speckles.

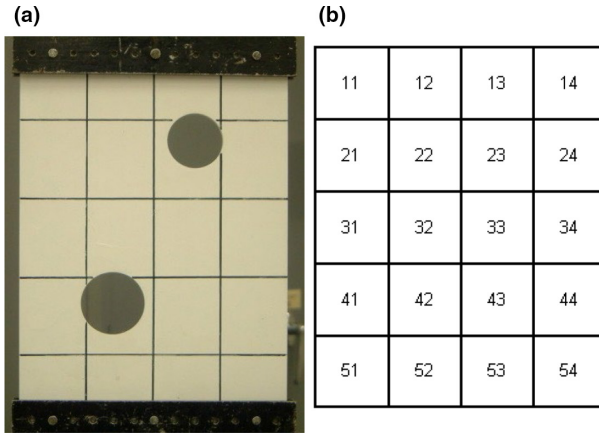


Figure 10: (a) Subdivided specimen and (b) region numbering scheme (row and column).

the two different tensile loads of 500 and 100 lb. By implementing the specimen domain decomposition into equally spaced subdomains, the resolution was improved to 0.027 mm/pixel, which could be further improved simply using a camera with higher resolution. After all the images were stored under both tensile loading conditions, the GA-based correlation technique was employed to compare the image intensity matrices and estimate the displacements.

#### 4 RESULTS AND DISCUSSION

The results obtained from each subdomain are assembled as shown in Fig. 11 and the final deformation gradient was obtained.

At the interface between different subdomains the information is unknown, and the equations of elastostatic compatibility were not satisfied. This was resolved by computationally integrating the various blocks and averaging the intensity of the nodes at the edges between neighboring subdomains along the median coordinate between the edges using an RBF interpolation technique. This resulted in a displacement distribution of the overall specimen as a single entity and not a compilation of several mismatching subdomain displacements. This methodology included the superposition of the boundaries of the holes where a smooth displacement field distribution is also obtained.

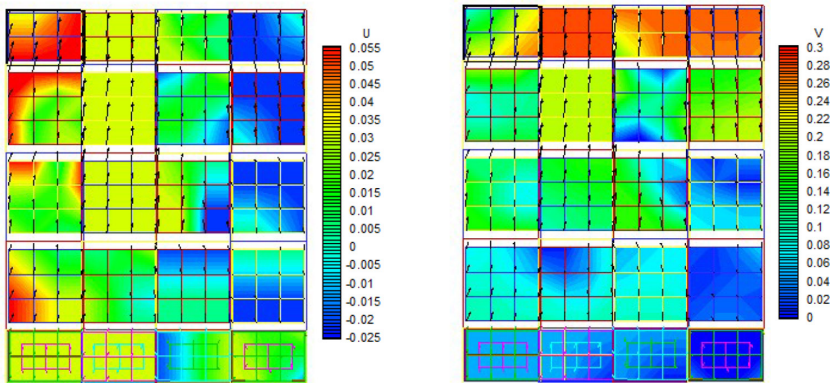


Figure 11: Displacement distribution of displacement components  $u$  and  $v$  from the genetic algorithm.

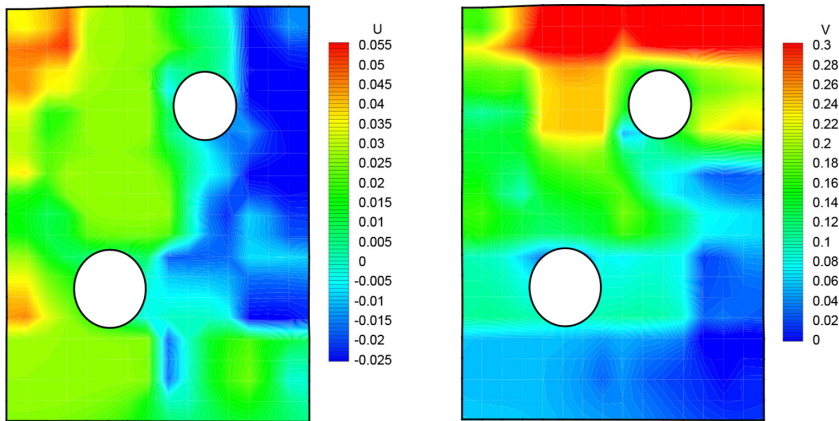


Figure 12: Displacement distribution of  $u$  and  $v$  at 10X magnification obtained from the integrated genetic algorithm.

The experimental results were validated against BEM simulations. The material property of the Plexiglas specimen was specified as shear modulus  $G = 1.030$  GPa. As the 2D BEM formulation is based on the principle of plane strain, the Poisson’s ratio was modified to  $\nu = 0.2668$  to match the actual test case. The boundary of the test specimen was discretized with 168 quadratic isoparametric discontinuous boundary elements while the holes were discretized each with 28 quadratic isoparametric discontinuous boundary elements. For the BEM models the bottom boundary was clamped, while a traction load of  $2.75$  N/mm<sup>2</sup> was applied on the top boundary of the specimen to match the 500-lb load. The left and right boundaries, as well as the edges of the holes, were traction-free.

Figures 12 and 13 show the  $x$  and  $y$  displacement field distribution plots magnified by a factor of 10 as compared with the solution obtained from BEM simulations. The results reveal reasonable qualitative agreement between the experimental and BEM results with

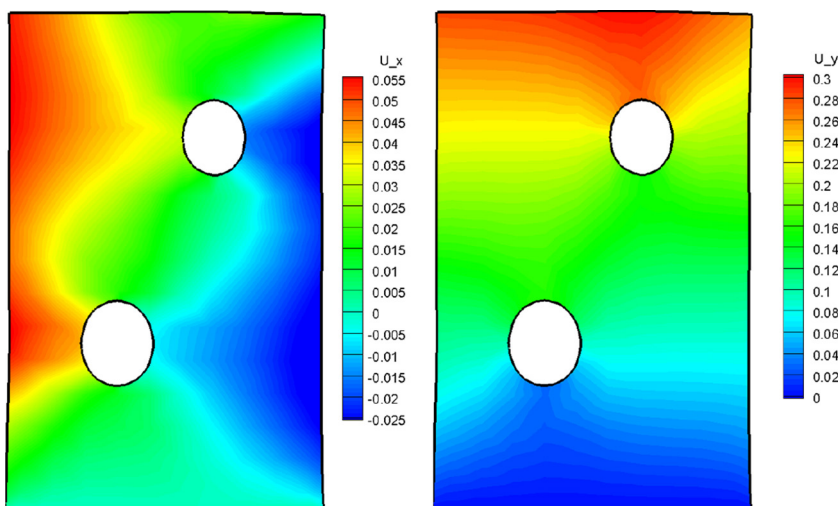


Figure 13: Displacement distribution of  $u$  ( $U_x$ ) and  $v$  ( $U_y$ ) computed using boundary element method.

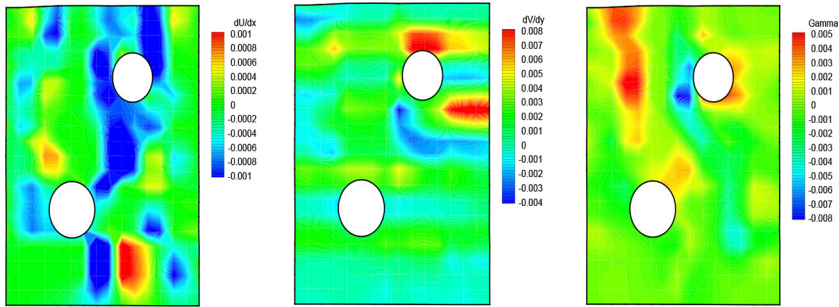


Figure 14: Strains components  $\epsilon_x$ ,  $\epsilon_y$ , and  $\gamma_{xy}$  distribution obtained by radial basis function interpolation.

general features of the displacement field distribution as well as the maximum values of the  $x$  and  $y$  displacements being properly captured by the experimental methodology.

Using RBF-FD differentiation scheme and its distribution, the strain components  $\epsilon_x$ ,  $\epsilon_y$ , and  $\gamma_{xy}$  were computed as shown in Fig. 14.

## 5 CONCLUSION

The GA-based DIC technique was successfully applied to measure surface displacements in structures using LSP. With readily available high-resolution digital cameras, the sensitivity of this technique can be significantly increased. A major advantage of this technique is its ability to subdivide the domain and hence use the full camera resolution in a small region. In addition, the GA was used to compute only the displacement components, which makes the technique more efficient. This is complemented by the RBF implementation to accurately compute the strain components. The technique is completely noncontact and highly accurate even for very small displacements as shown in the validation study conducted by the BEM simulations.

## REFERENCES

- [1] Manthey, D.W. & Lee, D., Vision based Surface Strain Measurement System. *JOM*, **47**(7), pp. 46–49, 1995. <https://doi.org/10.1007/bf03221231>
- [2] Vogel, J.H., & Lee, D., The automated measurement of strain from three-dimensional deformed surfaces. *JOM*, **42**(2), pp. 8–13, 1990. <https://doi.org/10.1007/bf03220863>
- [3] Theocaris, P.S., *Moiré Fringes in Strain Analysis*, Oxford: Pergamon Press, 1969.
- [4] Durelli, A.J. & Parks, V.J., *Moiré Analysis of Strain*, Prentice-Hall, 1970.
- [5] Chiang, F.P., *Experimental Stress Analysis Techniques* SESA Monograph, edited by A.S. Kobayashi, Chap.6, 1978
- [6] Vest, C.M., *Holographic Interferometry*, John Wiley and Sons, 1979.
- [7] Erf, R.K., *Speckle Metrology*, Academic Press, New York, 1978.
- [8] Kobayashi, A.S., *Handbook on experimental Mechanics*, VCH Publishers, New York, 1993.
- [9] Dainty, J.C., *Laser Speckle and Related Phenomena*, Springer-Verlag, New York, 1975
- [10] Takaki, T., et al., Strain visualization sticker using Moiré fringe for remote sensing, *Proceeding of the sixth international conference on bridge maintenance, safety and management*, pp. 8–12, 2012.
- [11] Han, B., Higher sensitivity moiré interferometry for micromechanical studies. *Optical Engineering*, **31**(7), pp. 1517–1526, 1992. <https://doi.org/10.1117/12.57681>

- [12] Huntley, J. M., Palmer, S.J.P., Goldrein, H. T. & Melin, L.G., Microstructural strain analysis by high magnification moiré interferometry. *SPIE Proceedings* (2545) (Interferometry VII: Applications), San Diego, USA, pp. 86–95, 1995.
- [13] Trolinger, J.D., Fundamentals of Interferometry and Holography for Civil and Structural Engineering Measurements. *Optics and Lasers in Engineering*, **24**(2–3), pp. 89–109, 1996. [https://doi.org/10.1016/0143-8166\(95\)00026-7](https://doi.org/10.1016/0143-8166(95)00026-7)
- [14] Rastogi, P. (ed.), *Photomechanics*, Springer-Verlag: Berlin Heidelberg, pp. 103–145, 2000.
- [15] Francis, D., Tatam, R.P. & Groves, R.M., Shearography technology and application: a review. *Measurement Science and Technology*, **21**(10), pp. 102001–102030. <https://doi.org/10.1088/0957-0233/21/10/102001>
- [16] Sutton, M.A., & Wolters, W.J., Determination of displacement using an improved digital image correlation method, *Image Vision Computing*, **1**(3), pp. 133–139, 1983. [https://doi.org/10.1016/0262-8856\(83\)90064-1](https://doi.org/10.1016/0262-8856(83)90064-1)
- [17] Chu, T.C., Ranson, W.F., Sutton, M.A., & Peters, W.H., Application of digital image correlation techniques to experimental mechanics, *Experimental Mechanics*, **25**, pp. 232–244, 1985. <https://doi.org/10.1007/bf02325092>
- [18] Sutton, M. A., Orteu, J.J., Schreier, H., *Image Correlation for Shape, Motion and Deformation Measurements*. Springer-Verlag: US, pp.
- [19] Bing, P., Hui-min, X., Bo-qin, X., Fu-long, D., Performance of sub-pixel registration algorithms in digital image correlation. *Measurement Science and Technology*, **17**(6), pp. 1615–1621, 2006. <https://doi.org/10.1088/0957-0233/17/6/045>
- [20] Mudassar, A.A., Butt, S., Improved Digital Image Correlation method. *Optics and Lasers in Engineering*, **87**, pp. 156–167, 2016. <https://doi.org/10.1016/j.optlaseng.2015.10.002>
- [21] Zhang, D.S., Luo, M., Arola, D.D., Displacement/strain measurements using an optical microscope and digital image correlation. *Optical Engineering*, **45**(3), 2006. <https://doi.org/10.1117/1.2182108>
- [22] Sutton, M.A, Li, N., Joy, D.C. & Reynolds, A.P., Scanning electron microscopy for quantitative small and large deformation measurements Part I: SEM imaging at magnifications from 200 to 10,000. *Experimental Mechanics*, **47**, pp. 775–787, 2007. <https://doi.org/10.1007/s11340-007-9042-z>
- [23] Yoneyama, S., Kikuta, H., Kitagawa, A. & Kitamura, K., Lens distortion correction for digital image correlation by measuring rigid body displacement. *Optical Engineering*, **45**(2), 2006. <https://doi.org/10.1117/1.2168411>
- [24] Sutton, M.A., et al., Metrology in a scanning electron microscope: Theoretical developments and experimental validation. *Measurement Science and Technology*, **17**(10), pp. 2613–2622, 2006. <https://doi.org/10.1088/0957-0233/17/10/012>
- [25] Sutton, M.A., et al., Scanning electron microscope for quantitative small and large deformation measurements part II, Experimental validation for magnifications from 200 to 10,000. *Experimental Mechanics*, **47**(6), pp. 789–804, 2007. <https://doi.org/10.1007/s11340-007-9041-0>
- [26] Sun, Y. & Pang, J.H.L., AFM image reconstruction for deformation measurements by digital image correlation. *Nanotechnology*, **17**(4), pp. 933–939, 2006. <https://doi.org/10.1088/0957-4484/17/4/016>
- [27] Gauvin, C., Jullien, D., Doumalin, P., Dupre, J.C. & Gril, J., Image correlation to evaluate the influence of hygrothermal loading on wood. *Strain*, **50**, pp. 428–435, 2014. <https://doi.org/10.1111/str.12090>

- [28] Pan, B., Reliability-guided digital image correlation for image deformation measurement. *Applied Optics*, **48(8)**, pp. 1535–1542, 2009. <https://doi.org/10.1364/ao.48.001535>
- [29] Yang, X., Liu, Z. & Xie, H., A real time deformation evaluation method for surface and interface of thermal barrier coatings during 1100 °C thermal shock. *Measurement Science and Technology*, **23(10)**, pp. 105604–105614, 2012. <https://doi.org/10.1088/0957-0233/23/10/105604>
- [30] Brillaud, J. & Lagattu, F., Limits and possibilities laser speckle and white-light image-correlation methods: Theory and experiments. *Applied Optics*, **41(31)**, pp. 6603–6613, 2002. <https://doi.org/10.1364/ao.41.006603>
- [31] Song, J., Yang, J., Liu, F. & Lu, K., Quality assessment of Laser speckle patterns for digital image correlation by a Multi Factor Fusion Index. *Optical Engineering*, **124**, pp. 105822–105837, 2020. <https://doi.org/10.1016/j.optlaseng.2019.105822>
- [32] Goodman, J.W., Laser speckle and related phenomena. *Statistical Properties of Laser Speckle Patterns*, **9**, pp. 9–75, 1975.
- [33] Kassab, A.J., Moslehy, F.A. & Daryapurkar, A., Detection of cavities by an inverse elastostatics boundary element method: experimental results. *Transactions of Modelling and Simulation*, **8**, pp. 85–92, 1994. [https://doi.org/10.1016/0955-7997\(94\)90006-x](https://doi.org/10.1016/0955-7997(94)90006-x)
- [34] Fraley, J.E., Hamed, M.A., Peters, W.H. & Ranson, W.F., Experimental boundary integral equation application in speckle interferometry. *SESA Spring Conference*, pp. 68–71, 1981.
- [35] Peters, W.H. & Ranson, W.F., Digital imaging techniques in experimental stress analysis. *Optical Engineering*, **21**, pp. 427–431, 1982.
- [36] Pilch, A., Maudlin, J., Mahajan, A. & Chu, T., Intelligent image correlation using genetic algorithms for measuring surface displacements and strain profiles. ASME International Mechanical Engineering Congress and Exposition, DSC-Volume **70**, pp. 81–88, 2001.
- [37] Chu, T., Mahajan, A. & Liu, C.T., An economical vision-based method to obtain all-field deformation profiles. *Experimental Techniques*, **26(6)**, pp. 25–29. <https://doi.org/10.1111/j.1747-1567.2002.tb00087.x>
- [38] Goldberg, D.E., *Genetic Algorithms in Search, Optimization and Machine Learning*. Addison-Wesley, Reading, MA, 1989.
- [39] Divo, E.A., Kassab, A.J. & Rodríguez, F., An efficient singular superposition technique for cavity detection and shape optimization. *Numerical Heat Transfer, Part B: Fundamentals*, **46(1)**, pp. 1–30, 2004. <https://doi.org/10.1080/10407790490436624>
- [40] Divo, E., Kassab, A. & Rodríguez, F., Characterization of space dependent thermal conductivity with a BEM based Genetic Algorithm. *Numerical Heat Transfer, Part A: Applications*, **37(8)**, pp. 845–875, 2000. <https://doi.org/10.1080/10407790490436624>
- [41] Silieti, M., Divo, E., & Kassab, A.J., Singular superposition/boundary element method for reconstruction of multi-dimensional heat flux distributions with applications to film cooling holes. *Computers, Materials and Continua*, **12(2)**, pp. 121–144, 2009.
- [42] Hardy, R.L., Multiquadric equations of topography and other irregular surfaces. *Journal of Geophysical Research*, **76(8)**, pp. 1905–1915, 1971.
- [43] Buhmann, M.D., *Radial Basis Functions: Theory and Implementation*. Cambridge University Press, Cambridge, 2003.
- [44] Kansa, E.J., Hon, Y.C., Circumventing the ill-conditioning problem with multiquadric radial basis functions: Applications to elliptical partial differential equations. *Computers & Mathematics with Applications*, **39(7–8)**, pp. 123–137, 2000.

- [45] Pepper, D., Kassab, A. & Divo, E., (eds.), *Introduction to Finite Element, Boundary Element and meshless methods: With Applications to Heat Transfer and Fluid Flow*, ASME Press.
- [46] Sarler, B., Tran-Cong, T. & Chen, C.S., Meshfree direct and indirect local radial basis function collocation formulations for transport phenomena. *WIT transactions on Modelling and Simulation*, pp. 417–427, 2005.
- [47] Brebbia, C.A., Telles, J.C.F. & Wrobel, L.C. (eds.), *Boundary Element Techniques*. Springer-Verlag: Berlin; 1984.
- [48] Gamez, B., Ojeda, D., Divo, E., Kassab, A. & Cerrolaza, M., Parallelized iterative domain decomposition boundary element method for thermoelasticity in piecewise non-homogeneous media. *Engineering Analysis with Boundary Elements*, **32**, pp. 1061–1073, 2008.
- [49] Ojeda, D., Gamez, B., Divo, E., Kassab, A. & Cerrolaza, M., Singular superposition elastostatics BEM/GA algorithm for cavity detection. *Boundary Elements and Other Mesh Reduction Methods XXIX*, **44**, pp. 313–322, 2007.